



LAWRENCE
LIVERMORE
NATIONAL
LABORATORY

Simultaneous In Situ Synthesis and Characterization of Co@Cu Core-Shell Nanoparticle Arrays

J. T. McKeown, Y. Wu, J. D. Fowlkes, P. D. Rack,
G. H. Campbell

September 10, 2014

Advanced Materials

Disclaimer

This document was prepared as an account of work sponsored by an agency of the United States government. Neither the United States government nor Lawrence Livermore National Security, LLC, nor any of their employees makes any warranty, expressed or implied, or assumes any legal liability or responsibility for the accuracy, completeness, or usefulness of any information, apparatus, product, or process disclosed, or represents that its use would not infringe privately owned rights. Reference herein to any specific commercial product, process, or service by trade name, trademark, manufacturer, or otherwise does not necessarily constitute or imply its endorsement, recommendation, or favoring by the United States government or Lawrence Livermore National Security, LLC. The views and opinions of authors expressed herein do not necessarily state or reflect those of the United States government or Lawrence Livermore National Security, LLC, and shall not be used for advertising or product endorsement purposes.

Simultaneous *In Situ* Synthesis and Characterization of Co@Cu Core-Shell Nanoparticle Arrays

Joseph T. McKeown^{1,*}, Yueying Wu², Jason D. Fowlkes³,
Philip D. Rack^{2,3}, and Geoffrey H. Campbell¹

Core-shell nanostructures have attracted much attention due to their unique and tunable properties relative to bulk structures of the same materials, making core-shell nanoparticles candidates for a variety of applications with multiple functionalities^{1,2}. Intriguing magnetic behavior can be tailored by variation of size, interface, crystal orientation, and composition, and core-shell nanostructures with noble-metal shells yield novel optical responses³ and enhanced electrocatalytic activity⁴. The immiscible Co-Cu alloy system is of particular interest, because it combines a strong magnet (Co) with an effective conductor (Cu)⁵ that has a tunable plasmonic resonance⁶. In this work, we present a method to synthesize Co@Cu nanoparticles via pulsed-laser-induced dewetting of Co-Cu alloy thin films. We show that this technique effectively synthesizes Co@Cu core-shell nanoparticles with controllable sizes ranging from tens to several hundred nanometers. Moreover, this bottom-up self-assembly process has the potential advantage to control the size and spacing of resultant nanoparticle arrays by exploiting a spontaneous thin-film instability^{7,8} that governs the liquid-phase dewetting process (requiring no lithographic patterning) or by a confluence of lithography and self-assembly for higher-order directed assembly^{9,10}.

Self-assembled nanoparticle arrays with unique properties have been obtained via solid- or liquid-state dewetting of metallic thin films at elevated temperatures⁸⁻¹². This self-assembly technique has the advantage of simplicity, high throughput, and low cost, resulting in nanoparticles with correlated size and spacing due to two-dimensional (2D) thin-film instabilities^{8,12,13} and pseudo one-dimensional (1D) Rayleigh-Plateau instabilities⁹⁻¹¹. For the case of ultrathin quasi-infinite liquid metal films, dewetting is typically dominated by the spinodal dewetting mechanism^{7,8}, described as rupturing of the film by amplification of unstable surface

¹ Condensed Matter and Materials Division, Lawrence Livermore National Laboratory, Livermore, CA 94550, USA, ²Department of Materials Science and Engineering, University of Tennessee, Knoxville, TN 37996, USA, ³Center for Nanophase Materials Science, Oak Ridge National Laboratory, Oak Ridge, TN 37831, USA.

* e-mail: mckeown3@llnl.gov

thermal fluctuations. This has been found to be the active mechanism during breakup of ultrathin, pure Cu^{7,8,11} and Co¹³ films on substrates. Spinodal dewetting results in particle spacings that are set by the fastest growing surface perturbation wavelengths, and the spatial characteristics of the final dewet film morphology are typically correlated with the initial film thickness to estimate an effective interface potential between the film and substrate^{7,8,12,14}. The dewetting dynamics, however, have been largely inferred from *ex situ* observations of the re-solidified metal quenched after different liquid lifetimes, as dewetting of thin metallic films occurs over nanosecond timescales^{8,14}. Recently, we captured *in situ* the dewetting dynamics of a thin Ni film using dynamic transmission electron microscopy¹², and the time and length scales were correlated to basic hydrodynamic theory.

When a driving force for chemical partitioning of an alloy thin film exists in tandem with a morphological instability that induces physical partitioning (or dewetting), as illustrated in Figure 1, ordered arrays of nanoparticles can be synthesized with fine-scale composition modulations that potentially provide enhanced functionality. Co-Cu alloys have negligible mutual solubility of Co and Cu below ~600 K, and the Co-Cu phase diagram displays a metastable liquid miscibility gap^{5,15,16}, where undercooled Co-Cu melts phase separate into a Co-rich liquid, L1, and a Cu-rich liquid, L2. The miscibility gap is approximately symmetric about 53at.%Cu, and the critical temperature for liquid phase separation was determined to be ~100 K below the liquidus line. Based on interfacial energy considerations, L1 is typically encapsulated by L2, and liquid Cu has been found to almost completely wet solid Co surfaces and perfectly wet high-angle Co grain boundaries near the peritectic temperature¹⁷ (1385 K). Here, we have investigated the nanoscale (time and length) self-assembly of equiatomic Co-Cu alloys *in situ* using the dynamic transmission electron microscope (DTEM)¹⁸⁻²⁰ in order to elucidate the dewetting dynamics that lead to core-shell nanoparticle formation. Based on *in situ* observations of the morphological evolution during dewetting of Co-Cu thin films combined with postmortem *ex situ* analyses of the resultant core-shell nanoparticles, the dewetting mechanisms, phase separation, and particle morphology are elucidated.

Approximately equiatomic, 10-nm-thick Co-Cu thin films were sputter-deposited onto 15-nm-thick silicon nitride membranes (see Methods). Based on TEM imaging and diffraction, the as-deposited thin films were determined to be nanocrystalline with an average grain size of ~12 nm (see Supplementary Information). Compositional analysis using energy-dispersive spectrometry (EDS) confirmed that the films were equiatomic.

Upon pulsed-laser heating, the Co-Cu films dewet the silicon nitride substrates. Figure 2 shows time-resolved images acquired during the pulsed-laser-induced dewetting process. The time labels in the images are the delays between the peak of the laser heating pulse and the electron imaging pulse at the specimen (see Methods for details). The time-delay series of images in Figure 2a and 2b were acquired from the center of the Gaussian laser heating pulse with total deposited energies of, respectively, 4.3 and 5.2 μJ . Inspection of these image series indicate different mechanisms for dewetting based on the morphology and timescales of film breakup. The approximate average particle size (diameter) and spacing for the resultant nanoparticle arrays (see Supplementary Information) in Figure 2a and 2b are, respectively, 160 nm with a spacing of 550 nm and 105 nm with a spacing of 275 nm. While it is difficult to state definitively the mechanism by which the films dewet²¹, the longer timescales associated with dewetting using lower energy (Figure 2a) are likely due to incomplete melting. Lower temperature and a solid phase would lead to longer timescales for dewetting. Based on the equilibrium phase diagram¹⁵ and the observed morphology in the time-resolved images, it is suggestive of a coexisting Co-rich solid phase and Cu-rich liquid phase during dewetting at lower laser energy. It is unlikely that a completely solid-state dewetting process was active, as the timescale for complete dewetting would be much longer than observed ($<1 \mu\text{s}$). The morphology of this film breakup is indicative of a nucleation and growth mechanism, where film rupturing occurred by random nucleation of holes that grew with time.

In contrast, the timescale for dewetting at higher laser energy (Figure 2b) is close to an order of magnitude shorter ($\sim 100 \text{ ns}$). The film breakup observed in the time-resolved images indicate a liquid-phase spinodal dewetting mechanism with a bicontinuous morphological pathway.⁷ Assuming that the measured particle spacing represents the wavelength of maximum growth (λ_m), the maximum perturbation growth rate (σ_m) can be estimated by:

$$\sigma_m = \frac{8\pi^4 \gamma h_0^3}{3\nu \lambda_m^4} \quad (1)$$

where γ is the liquid surface energy (for which we used $1.58 \text{ J/m}^{22,23}$), h_0 is the initial film thickness (10 nm), ν is the liquid viscosity (we used a value of $3.93 \times 10^{-3} \text{ Pa}\cdot\text{s}^{24,25}$), and λ_m is the measured particle spacing (275 nm). The spinodal timescale is then simply $\tau_m = 1/\sigma_m$, for which we calculate a value of $\tau_m = 55 \text{ ns}$. This is consistent with the time-resolved images in Figure 2b, given that there are likely competing Rayleigh-Plateau instabilities⁹⁻¹¹ that are active when the

liquid film breaks up into the intermediate rivulet morphology as well as thermocapillary and surface tension effects that can lead to deviations from linear spinodal theory^{21,26,27}.

Irrespective of the laser energy and active dewetting mechanism, the resultant dewet arrays are comprised of Co@Cu core-shell nanoparticles, as shown in the energy-filtered TEM (EFTEM) images of Figure 2. Zero-loss images and composition maps are provided for both the low and high laser energy time-delay series in Figure 2a and 2b (see Methods for details). A distribution of particle sizes is evident in these images, with smaller particles being comprised mainly of Co. The areal density of these smaller particles decreases with increased laser energy, and this is likely attributable to lower surface mobility of both atomic species at lower temperature and particularly of Co in the solid state (as in Figure 2a). The core-shell nanoparticles clearly consist of a Co-rich core surrounded by a Cu-rich shell, resulting from the lower surface tension of liquid Cu relative to both solid and liquid Co^{5,15,16,22}. In the case of coexisting solid Co-rich and liquid Cu-rich phases (lower laser energy), the Cu-rich liquid will have a lower interface energy with the silicon nitride and will wet the Co-rich solid, as has been shown in prior studies¹⁷. For the case of complete melting (higher laser energy), undercooling to a temperature below the critical temperature of the liquid miscibility gap leads to encapsulation of Co-rich L1 by Cu-rich L2 due to surface tension considerations^{15,16}. Given the nanoscale experimental geometry and the observed timescales for dewetting, it is likely that large undercoolings are present in the melt and the liquid is well below the critical temperature. It has also been shown that the Co-rich L1 phase typically solidifies first¹⁵, which would again yield a solid Co-rich phase that is wet by the Cu-rich L2 liquid.

Figure 3 provides a time-delay series of images acquired at a radius of $\sim 35\ \mu\text{m}$ from the center of the incident laser pulse (the diameter of the region of film that dewets the substrate upon laser heating is $\sim 70\ \mu\text{m}$) as a 10-nm-thick Co-Cu film dewets a silicon nitride substrate. The total deposited energy was $5.2\ \mu\text{J}$. The morphology and timescale of film breakup are again suggestive of a coexisting Co-rich solid phase and Cu-rich liquid phase during dewetting, as in Figure 2a, where film rupturing and dewetting occurred by nucleation and growth of holes. This was due to the lower laser fluence at larger radii that results from the Gaussian spatial profile of the laser pulse. In the images shown in Figure 3, the laser intensity (and thus temporal evolution of dewetting and nanoparticle formation) varies with radial position from lower intensity at larger radius to higher intensity at smaller radius (left to right in the DTEM images, upper left to lower right in the EFTEM montage images). While the DTEM images show

intermediate stages of hole formation and coalescence to form pseudo-linear wire morphologies that subsequently break up, the EFTEM images reveal the temporal evolution of the chemical instability and core-shell nanoparticle formation. As holes nucleate and coalesce in the film, the Co and Cu phase separate due to their mutual immiscibility, as seen in the EFTEM composition map at larger radius. However, as is evident in the EFTEM maps, the Co-rich phase continues to coalesce and moves to the interiors of particles and rivulets (i.e., the Cu-rich phase surrounds the Co-rich phase), eventually resulting in Co@Cu core-shell nanoparticles (as seen in the lower right of Figure 3). The surface energy of Cu is lower than the surface energy of Co in both the solid and liquid phases at all relevant temperatures^{5,16,17,22,23,28}, and the observed morphological evolution that results in Co@Cu core-shell nanoparticles can be attributed to overall surface energy minimization and the short diffusion distances necessary to form core-shell structures.

The structure of the resultant nanoparticles was evaluated using imaging and diffraction in the TEM. Bright- and dark-field (BF, DF) TEM images and selected-area diffraction patterns (SADP) were obtained from two observed core-shell nanoparticle morphologies, as shown in Figure 4a and 4b, respectively. Twinning is evident in the BF and DF images of Figure 4b. Both SADPs were acquired with the nanoparticles in a $[1\bar{1}0]$ zone-axis orientation relative to the incident electron beam. The SADPs suggest single-crystalline nanoparticles, but the lattice parameters of Cu (3.615 Å) and α -Co (3.563), both fcc structures, are very similar and the diffraction patterns overlap with a distinct crystallographic orientation relationship between the two phases. From these diffraction patterns, the orientation relationship can be defined as: $(002)[1\bar{1}0]_{\text{Cu}} \parallel (002)[1\bar{1}0]_{\alpha\text{-Co}}$. This cube-cube orientation relationship is consistent with that of nanoscale Co precipitates found in rapidly solidified, melt-spun Co-Cu ribbons²⁹, where coherent interfaces are maintained between the Co precipitates and Cu matrix with a cube-cube relationship, as well as with Monte Carlo simulations of phase separation behavior in Co-Cu nanoparticles³⁰. The SADP in Figure 4b clearly shows the $\{111\}$ -type twin planes, as expected for fcc metals.

In conclusion, through a combination of morphological and chemical instabilities an initially continuous, quasi-infinite thin film self-assembles and phase separates into Co@Cu core-shell nanoparticle arrays. The synthesis of these nanoparticle arrays was monitored with nanoscale spatial and temporal resolutions, which, when combined with *ex situ* composition analysis, provided insight to the morphological and chemical evolution pathways leading to

core-shell nanoparticle formation. Controlling these instabilities can potentially lead to ordered arrays of nanoparticles with enhanced functionality through directed self-assembly, and characterization of the mechanisms that govern these dynamic self-organization processes at the relevant spatial and temporal scales represents a key challenge toward realizing the goal of engineering nanoscale systems and devices for a variety of technological applications.

Methods

Approximately equiatomic Co-Cu alloy films with a thickness of 10 nm were RF magnetron sputter-deposited onto 15-nm-thick silicon nitride TEM membranes (Ted Pella, Inc., Redding, CA). The films were co-sputtered from individual 50-cm-diameter Cu and Co targets at room temperature and 5 mTorr Ar pressure using a flow rate of 25 sccm. To produce the equiatomic composition, the Cu and Co sputtering rates were both calibrated to a 2 nm/min deposition rate, which required 30 and 69 W applied to the targets, respectively.

In-situ dewetting experiments were conducted in the DTEM at Lawrence Livermore National Laboratory operating at 200 kV in both single-shot mode¹⁸⁻²⁰ and Movie Mode^{20,31}. The thermal stimulus to drive dewetting was delivered using a 1064-nm wavelength, ~15-ns pulsed Nd:YAG laser with a Gaussian beam profile ($1/e^2$ diameter of $135 \pm 5 \mu\text{m}$) incident at 45° to the film normal. Total deposited energies of 4.3 and 5.2 μJ were used, corresponding to laser fluences of ~30 and 36 mJ/cm^2 , respectively. The imaging electron pulses were generated at a preset delay time relative to the laser-heating pulse. In single-shot mode, a 15-ns electron pulse was generated using a Nd:YLF laser that was frequency quintupled to 211 nm. In Movie Mode, photo-emitted electron pulses were generated with a fiber-based Nd:YAG laser converted to 5th harmonic (213 nm) incident on the TEM cathode. The laser pulse train was delivered to the TEM photocathode with precise temporal spacing and shaping, resulting in multiple photo-emitted electron pulses of $\sim 10^9$ electrons. An electrostatic deflector installed beneath the electron optics in the TEM column shifts each image to a different part of the CCD detector. The 9 images were captured in a single exposure of the CCD camera, circumventing the ~ms temporal limit on the refresh rate of the camera. For these dewetting studies, pulse trains consisted of 9 20-ns pulses with either 75- or 200-ns inter-pulse spacings. In both acquisition modes, the duration of the electron pulse (15 or 20 ns) represents the temporal resolution of the DTEM imaging experiments, and the images are time-averaged over the duration of the electron pulse. Regardless of the DTEM acquisition mode, all time-delay image series acquired

from the center of the Gaussian laser pulse (Figure 2) must be considered as ensemble-average pictures of dewetting, as it is difficult to capture a complete dewetting event in a single experiment due to the associated short timescales. The time-delay image series in Figure 3 is a single experiment.

The alloy thin films were characterized by TEM analyses before and after laser-heating and dewetting experiments in the DTEM. TEM was conducted on a Philips CM300 FEG (S)TEM operating at an accelerating voltage of 300 kV. The TEM is equipped with a Gatan Imaging Filter (GIF) and an X-ray energy dispersive spectrometer (Oxford Instruments). Elemental maps were acquired by energy-filtered TEM (EFTEM) using the Co and Cu $L_{2,3}$ edges. The respective $L_{2,3}$ onset edges for Co and Cu are 739 and 931 eV.

References

1. Schärftl, W. Current directions in core-shell nanoparticle design. *Nanoscale* **2**, 829-843 (2010).
2. Wei, S. *et al.* Multifunctional composite core-shell nanoparticles. *Nanoscale* **3**, 4474-4502 (2011).
3. Guo, Z., Henry, L. L. & Podlaha, E. J. An examination of Co and Fe nanoparticles with a protecting shell. *ECS Trans.* **1**, 63-69 (2006).
4. Ahmed, J. *et al.* Enhanced electrocatalytic activity of copper-cobalt nanostructures. *J. Phys. Chem. C* **115**, 14526-14533 (2011).
5. Egry, I. *et al.* Surface tension, phase separation, and solidification of undercooled Cobalt-Copper alloys. *Adv. Eng. Mater.* **5**, 819-823 (2003).
6. Wu, Y., Fowlkes, J. D. & Rack, P. D. The optical properties of Cu-Ni nanoparticles produced via pulsed laser dewetting of ultrathin films: The effect of nanoparticle size and composition on the plasmon response. *J. Mater. Res.* **26**, 277-287 (2011).
7. Bischof, J., Scherer, D., Herminghaus, S. & Leiderer, P. Dewetting modes of thin metallic films: Nucleation of holes and spinodal dewetting. *Phys. Rev. Lett.* **77**, 1536 (1996).
8. Herminghaus, S. *et al.* Spinodal dewetting in liquid crystal and liquid metal films. *Science* **282**, 916-919 (1998).
9. Rack, P. D., Guan, Y., Fowlkes, J. D., Melechko, A. V. & Simpson, M. L. Pulsed laser dewetting of patterned thin metal films: A means of directed assembly. *Appl. Phys. Lett.* **92**, 223108 (2008).
10. Fowlkes, J. D., Kondic, L., Diez, J. A., Wu, Y. Y. & Rack, P. D. Self-assembly versus directed assembly of nanoparticles via pulsed laser induced dewetting of patterned metal films. *Nano Lett.* **11**, 2478-2485 (2011).
11. Wu, Y. Y. *et al.* Competing liquid phase instabilities during pulsed laser induced self-assembly of copper rings into ordered nanoparticle arrays on SiO₂. *Langmuir* **27**, 13314-13323 (2011).

12. McKeown, J. T. *et al.* Real-time observation of nanosecond liquid-phase assembly of nickel nanoparticles via pulsed-laser heating. *Langmuir* **28**, 17168-17175 (2012).
13. Trice, J., Thomas, D., Favazza, C., Sureshkumar, R. & Kalyanaraman, R. Pulsed-laser-induced dewetting in nanoscopic metal films: Theory and experiments. *Phys. Rev. B* **75**, 235439 (2007).
14. Kalyanaraman, R. *et al.* Self-organization of nanoscale multilayer liquid metal films: Experiment and theory. *ACS Nano* **5**, 470-476 (2011).
15. Cao, C. D., Görlér, G. P., Herlach, D. M. & Wei, B. Liquid-liquid phase separation in undercooled Co-Cu alloys. *Mater. Sci. Eng. A* **A325**, 503-510 (2002).
16. Antion, C. & Chatain, D. Liquid surface and liquid/liquid interface energies of binary subregular alloys and wetting transitions. *Surf. Sci.* **601**, 2232-2244 (2007).
17. Curiotto, S. & Chatain, D. Solid/liquid interface energy and wetting of Cu at Co surfaces and grain boundaries. *Scripta Mater.* **60**, 40-43 (2009).
18. Kim, J. S. *et al.* Imaging of transient structures using nanosecond in situ TEM. *Science* **321**, 1472-1475 (2008).
19. LaGrange, T. *et al.* Nanosecond time-resolved investigations using the in situ dynamic transmission electron microscope (DTEM). *Ultramicroscopy* **108**, 1441-1449 (2008).
20. LaGrange, T. *et al.* Approaches for ultrafast imaging of transient materials processes in the transmission electron microscope. *Micron* **43**, 1108-1120 (2012).
21. Nguyen, T. D., Fuentes-Cabrera, M., Fowlkes, J. D. & Rack, P. D. Coexistence of spinodal instability and thermal nucleation in thin-film rupture: Insights from molecular levels. *Phys. Rev. E* **89**, 032403 (2014).
22. Harrison, D. A., Yan, D. & Blairs, S. The surface tension of liquid copper. *J. Chem. Thermo.* **9**, 1111-1119 (1977).
23. Yao, W. J., Han, X. J., Chen, M., Wei, B. & Guo, Z. Y. Surface tension of undercooled liquid cobalt. *J. Phys. Condens. Matter* **14**, 7479-7485 (2002).
24. Assael, M. J. *et al.* Reference data for the density and viscosity of liquid copper and liquid tin. *J. Phys. Chem. Ref. Data* **39**, 033105 (2010).
25. Assael, M. J. *et al.* Reference data for the density and viscosity of liquid cadmium, cobalt, gallium, indium, mercury, silicon, thallium, and zinc. *J. Phys. Chem. Ref. Data* **41**, 033101 (2012).
26. Favazza, C., Kalyanaraman, R. & Sureshkumar, R. Dewetting of ultrathin metal films from pulsed laser melting. *Nanotechnology* **17** (2006).
27. Trice, N. *et al.* Novel self-organization mechanism in ultrathin liquid films: Theory and experiment. *Phys. Rev. Lett.* **101**, 017802 (2008).
28. Tyson, W. R. & Miller, W. A. Surface free energies of solid metals: Estimation from liquid surface tension measurements. *Surf. Sci.* **62**, 267-276 (1977).
29. Yang, G. Y., Zhu, J., Wang, W. D., Zhang, Z. & Zhu, F. W. Precipitation of nanoscale Co particles in a granular Cu-Co alloy with giant magnetoresistance. *Mater. Res. Bull.* **35**, 875-885 (2000).
30. Shim, J.-H., Lee, B.-J., Ahn, J.-P., Choo, Y. W. & Park, J.-K. Monte Carlo simulation of phase separation behavior in a Cu-Co alloy nanoparticle. *J. Mater. Res.* **17**, 925-928 (2002).

31. Santala, M. K. *et al.* Irreversible reactions studied with nanosecond transmission electron microscopy movies: Laser crystallization of phase change materials. *Appl. Phys. Lett.* **102**, 174105 (2013).

Acknowledgments

Work was performed under the auspices of the U.S. Department of Energy by Lawrence Livermore National Laboratory (LLNL) under Contract No. DE-AC52-07NA27344. Activities and personnel at LLNL were supported by the Office of Science, Office of Basic Energy Sciences, Division of Materials Sciences and Engineering of the U.S. Department of Energy under FWP SCW0974. Y. Wu and J. D. Fowlkes acknowledge support from the U.S. Department of Energy, Office of Science, Office of Basic Energy Sciences, Division of Materials Sciences and Engineering. P. D. Rack acknowledges support from NSF Grant No. CBET-1235651. The authors acknowledge that a portion of this work was conducted at the Center for Nanophase Materials Sciences, which is sponsored at Oak Ridge National Laboratory by the Office of Basic Energy Sciences of the U.S. Department of Energy.

Author contributions

P.D.R., J.D.F., and J.T.M. conceived and designed the experiments, Y.W. performed thin-film deposition, J.T.M. performed time-resolved imaging in the DTEM and subsequent TEM characterization of nanoparticle arrays, J.T.M. and Y.W. analyzed the data, J.T.M wrote the manuscript and prepared the figures. All authors discussed the results and commented on the manuscript. G.H.C. supervised the project at LLNL, P.D.R. supervised the project at ORNL and the University of Tennessee.

Additional information

Supplementary information is available in the online version of the paper. Reprints and permissions information is available online at www.nature.com/reprints. Correspondence and requests for materials should be addressed to J.T.M.

Competing financial interests

The authors declare no competing financial interests.

Figures

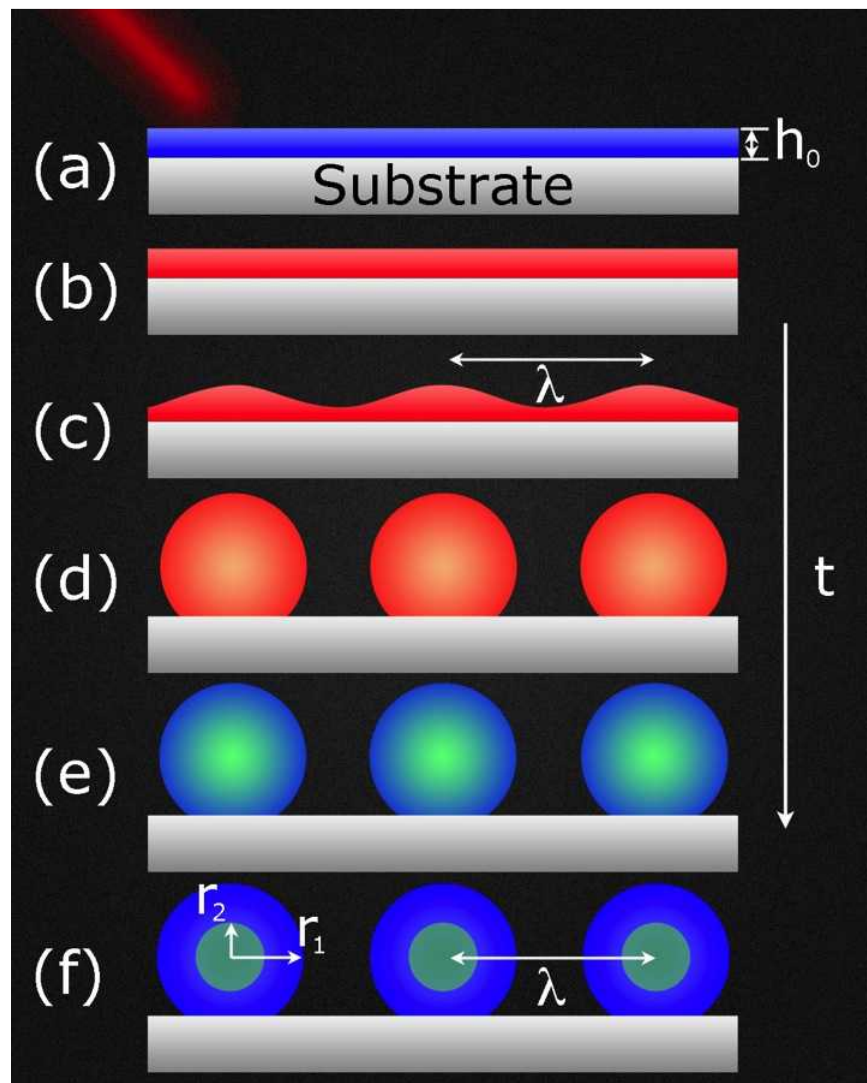


Figure 1 | Illustration of a morphological and chemical instability acting in tandem to produce core-shell nanoparticles. When **a**, a thin alloy film with initial thickness, h_0 , is laser-heated above the melting temperature of the alloy, **b**, the thin liquid film on the substrate may be unstable to surface thermal fluctuations, causing the film to **c**, break up with a characteristic spacing, λ (as in spinodal dewetting). **d**, **e**, Dewetting leads to arrays of nanoparticles that can potentially phase separate in both the liquid and solid states if a chemical driving force exists, leading to, for example, **f**, core-shell nanoparticle arrays of characteristic size (r) and spatial distribution (λ). In the figure, the arrow labeled “ t ” corresponds to increasing time.

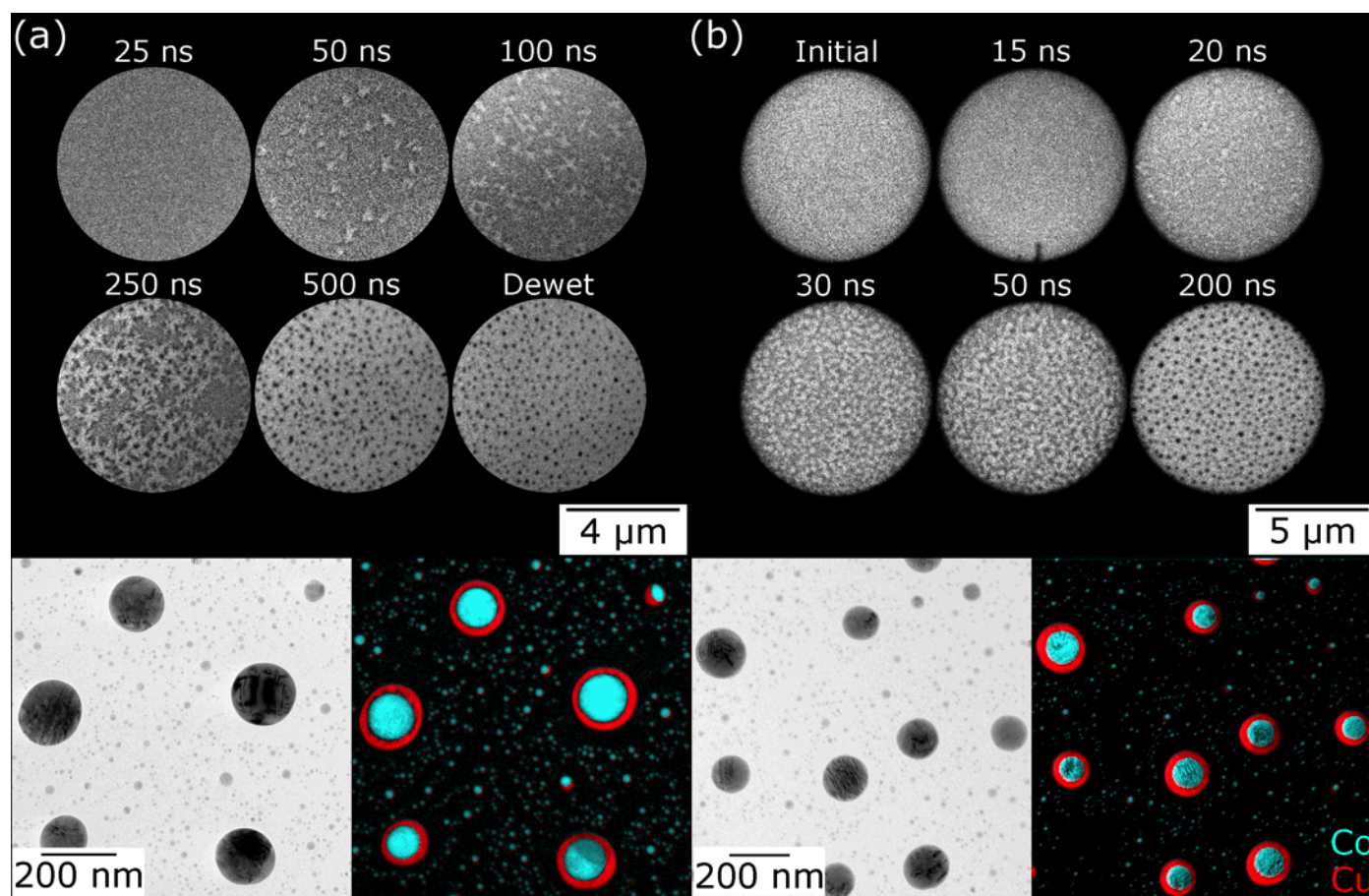


Figure 2 | *In situ* time-resolved imaging of dewetting via two mechanisms, with associated elemental maps of resultant core-shell nanoparticle arrays. Time-delay series of images as a 10-nm-thick Co-Cu film dewets a silicon nitride substrate. The image series in **a** and **b** were acquired at the center of the Gaussian laser heating pulse with total deposited energies of **a**, 4.3 μJ and **b**, 5.2 μJ . Beneath each of the time-delay series are EFTEM images of the resultant core-shell nanoparticles: zero-loss image and associated overlaid Co and Cu maps.

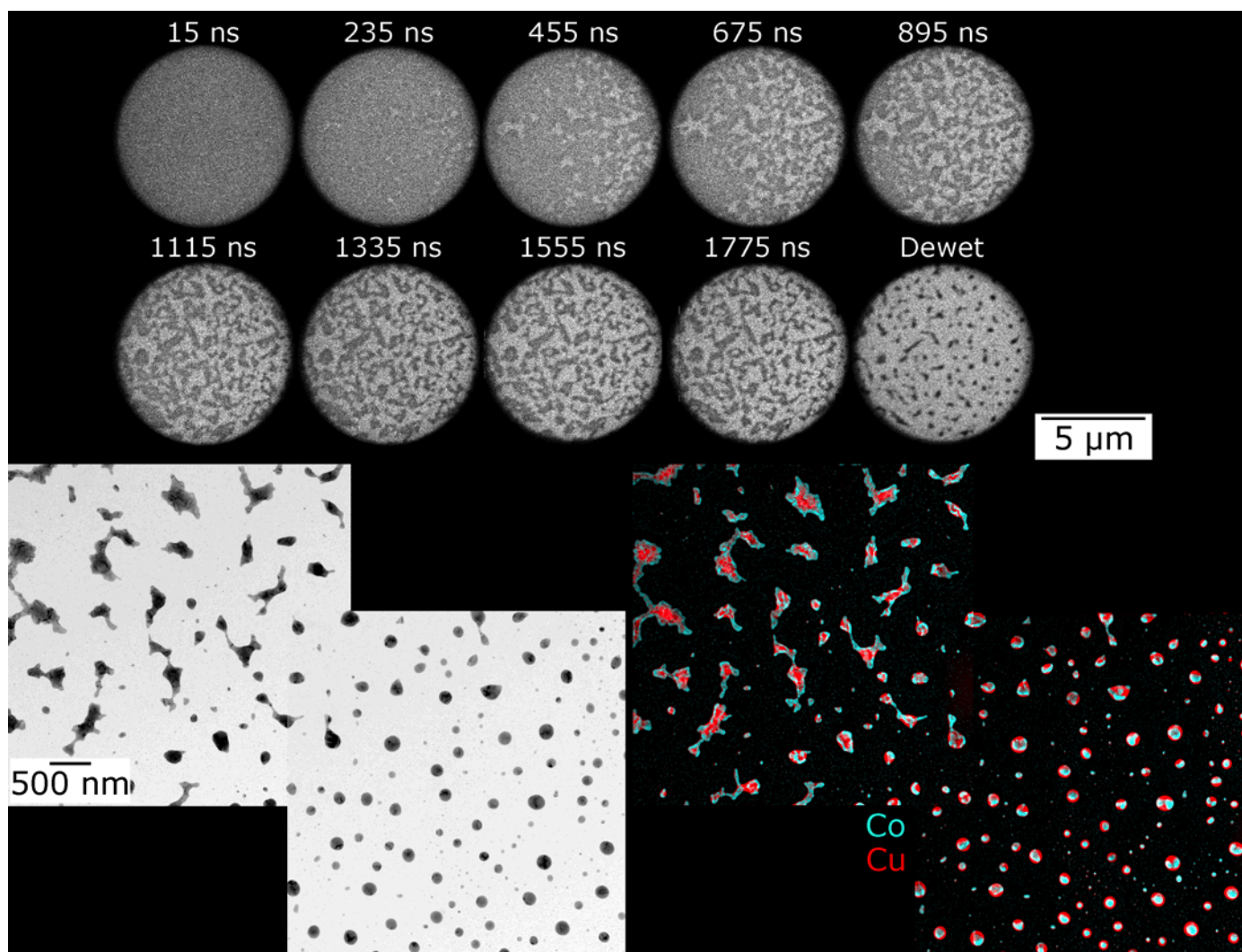


Figure 3| Combine *in situ* time-resolved and *ex situ* compositional characterization revealing the temporal evolution of core-shell nanoparticle formation. (Upper) Time-delay series of images as a 10-nm-thick Co-Cu film dewets at a radius of $\sim 35\ \mu\text{m}$ from the center of the Gaussian pulse with a total deposited energy of $5.2\ \mu\text{J}$. (Lower) EFTEM imaging of resultant nanostructure. The center of the Gaussian laser pulse (not in the image) is toward the lower right of the zero-loss montage image and composition map.

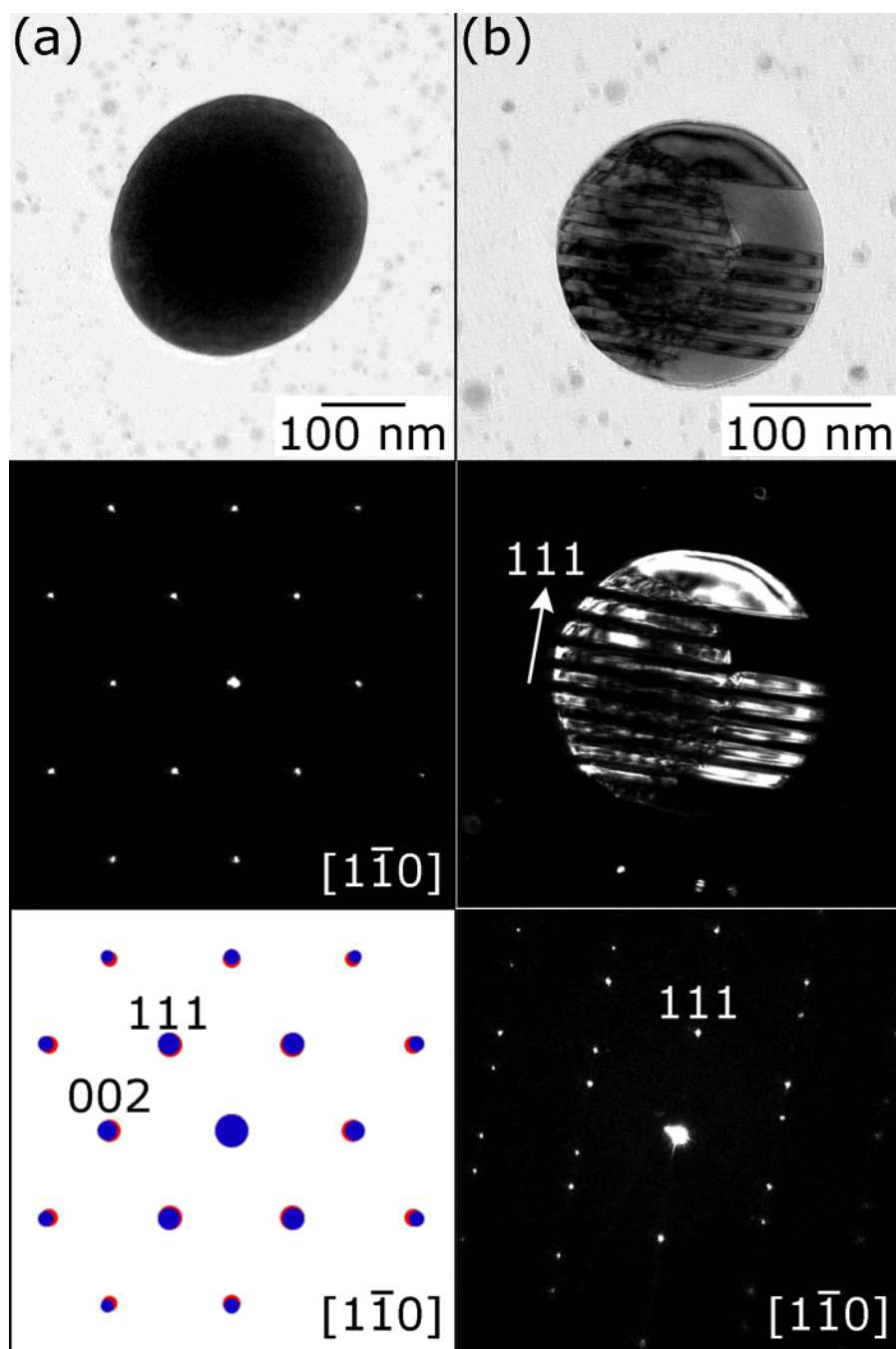


Figure 4 | Structural characterization of resultant core-shell nanoparticles. **a**, (Upper) BF TEM image of nanoparticle in (middle) $[1\ 0]$ zone-axis orientation, as shown in SADP, with (lower) simulated SADP showing OR between fcc Cu and fcc α -Co (Cu, red; Co, blue). **b**, (Upper, middle) BD and DF images of twinned nanoparticle, with (lower) SADP showing (111)-type twin planes.